SANDIA REPORT
SAND2020-10342
Printed September 2020

Sandia National Laboratories

Rapid Assessment of Autoignition Propensity in Novel Fuels and Blends

Leonid Sheps, Zachary J. Buras, Kendrew Au, Judit Zádor, Cosmin Safta

Prepared by
Sandia National Laboratories
Albuquerque, New Mexico
87185 and Livermore,
California 94550

Issued by Sandia National Laboratories, operated for the United States Department of Energy by National Technology & Engineering Solutions of Sandia, LLC.

Available to DOE and DOE contractors from
U.S. Department of Energy
Office of Scientific and Technical Information
P.O. Box 62
Oak Ridge, TN 37831

Telephone: (865) 576-8401
Facsimile: (865) 576-5728
E-Mail: reports@osti.gov
Online ordering: http://www.osti.gov/scitech

Available to the public from
U.S. Department of Commerce
National Technical Information Service
5301 Shawnee Rd
Alexandria, VA 22312

Telephone: (800) 553-6847
Facsimile: (703) 605-6900
E-Mail: orders@ntis.gov
Online order: https://classic.ntis.gov/help/order-methods/

ABSTRACT

We developed a computational strategy to correlate bulk combustion metrics of novel fuels and blends in the low-temperature autoignition regime with measurements of key combustion intermediates in a small-volume, dilute, high-pressure reactor. We used neural net analysis of a large simulation dataset to obtain an approximate correlation and proposed experimental and computational steps needed to refine such a predictive correlation. We also designed and constructed a high-pressure laboratory apparatus to conduct the proposed measurements and demonstrated its performance on three canonical fuels: n-heptane, i-octane, and dimethyl ether.

ACKNOWLEDGEMENTS

We would like to thank the following people for their help: Drs. David L. Osborn (8353), Nils Hansen (8353), and Craig Taatjes (8350) for thoughtful discussions and the use of some lab equipment; Erxiong Huang and Raybel Almeida (both in 8353) for helpful technical advice, Dr. Dario Lopez Pintor (8362) for useful discussions about fuel properties, Alberto Garica (8362) and Kent Smith (8351) for assistance with manufacturing custom parts, Greg de Bord (8351) for help with the use of computer clusters, and Drs. Scott Wagnon and Goutham Kukkadapu (LLNL) for providing reduced Co-Optima chemical mechanisms.

CONTENTS

1. Introduction 9
2. prediction of 1st-stage ignition delays based on chemical kinetics modeling 10
   2.1. Computational strategy 10
      2.1.1. Generation of simulation dataset 10
      2.1.2. Choosing an experimental platform for dilute oxidation measurements 11
      2.1.3. Simulations of 1st-stage IDT 12
      2.1.4. Statistical analysis of correlations 12
   2.2. Results 13
      2.2.1. Sorted cross-validation error test 13
      2.2.2. Leave-one-fuel-out test 15
      2.2.3. Choosing an appropriate measurement target 16
      2.2.4. Optimizing the design of measurements 17
   2.3. Summary 17
3. Construction of a high-pressure HPFR/FAGE apparatus. 19
   3.1. High-Pressure Flow Reactor. 19
      3.1.1. Construction of the rapid laminar gas mixer 20
      3.1.2. Temperature profile in the HPFR 21
      3.1.3. Fluid dynamics simulations of the HPFR 22
   3.2. FAGE detector 23
      3.2.1. FAGE operating modes 23
      3.2.2. Calibration of OH detection efficiency. 24
      3.2.3. Subtracting interference in OH measurements at operating conditions 26
4. First measurements of reactivity of representative fuels 27
   4.1. *n*-heptane 27
   4.2. *i*-octane 28
   4.3. DME 28
5. Conclusion/Outlook 29

LIST OF FIGURES

Figure 1: Key elementary reactions in autoignition. Radical chain branching steps are shown as red arrows, chain propagating steps in black, and chain inhibition steps in blue. 9
Figure 2: Schematic of CNN architecture used to find correlations between simulated flow reactor profiles and 1st-Stage IDT. The example simulations are for n-heptane at 600 K, 13.5 Bar. 13
Figure 3. Simulated profiles for oxidation of n-heptane at 600 K and 13.5 bar (left) and i-pentanol at 700 K and 20 bar (right) under flow reactor (top) and ignition delay time (bottom) conditions. 14
Figure 4: Predicted 1st-stage IDT (from OH/HO_2 FR training data) vs. explicitly simulated 1st-stage IDT. Combined results are shown for the sorted 10-fold CV test, in which the test data consisted of consecutive 10%-wide subsets of all simulations, in order of increasing 1st-stage IDT values (i.e. 0–10%, 10–20%, … 90–100%). Dashed lines represent factor of two errors. 15

Figure 5: Error distributions of predicted 1st-stage IDTs in the leave-one-fuel-out tests of the FR/IDT simulations. CNN was trained on FR profiles of OH/HO_2. 16
Figure 6: Effect of different inputs to the CNN: markers are 10-fold averaged CV error and the shaded area marks the minimum and maximum test errors of the folds. In the τ_{SO} case the DNN is trained only on T, P and τ_{SO} values, without product profiles input into the CNN. 17
Figure 7. Overview schematic of the HPFR/FAGE apparatus. *Top insert*: cartoon of the rapid fuel mixer in the HPFR. *Right insert*: cartoon of the sampled gas flow and laser-induced fluorescence probing in the FAGE. 19
Figure 8. *A*: schematic of the rapid laminar gas mixer. (Dimensions not to scale and only 7 needles are shown for illustration purposes.) *B*: photograph of front of the 1st prototype version of the mixer. 21
Figure 9. Temperature profiles under typical operating conditions at P = 13 bar in the HPFR with average residence times τ = 1 s (*left*) and 0.1 s (*right*). 21
Figure 10. Reduced velocity v_r (defined as the ratio of gas velocity to the average velocity) as a function of the spatial position in the HPFR at P = 13 bar and T = 600 K. The gas flow from the mixer at x = 40 mm to the sampling endwall at x = 0 mm is simulated for τ_{max} = 1 and 0.1 s. 22
Figure 11. Simulated centerline reduced velocity at P = 13 bar, T = 600 K, τ_{max} = 1 and 0.1 s....22
Figure 12. Representative OH time profiles measured using the Photolysis/LIF mode at total P = 1 bar (N_2) in the FAGE. Computed initial OH concentrations are $1.5 \cdot 10^{11}$ and $2.5 \cdot 10^{13}$ cm^{-3}. Solid lines are fits using the chemical model of Zhang et al. [55] 24
Figure 13. *Panel A*: Typical OH time profile, measured using the Photolysis/LIF mode at total P = 5 Torr (air) in the FAGE. Initial OH concentration is $3.6 \cdot 10^9$ cm^{-3}. *Panel B*: Summary of all OH calibration measurements at *T* = 300 – 600 K. 25
Figure 14. OH survival probability during sampling from HPFR as a function of total gas flow in the FAGE (sampling + co-flow). The survival probability is defined as the percentage of OH radicals, created by laser photolysis in the HPFR, that survive and are detected in the FAGE. Shown for comparison are models of OH transport through the FAGE cell with two values of the sticking coefficient for OH loss on the walls. 26
Figure 15. FR measurements in of *n*-heptane oxidation at *T* = 650 K, *P* = 13 bar, and τ_{max} = 0.2 s. The measured profiles of OH, HO_2, and H_2O_2 are plotted vs. axial injector position in units of absolute number density. The *n*-heptane profile is plotted relative to its initial concentration. 27
Figure 16. FR measurements in of *i*-octane oxidation at T = 650 K, P = 13 bar, and τ_{max} = 0.5 s. The measured profiles of OH and H_2O_2 are plotted vs. axial injector position in units of absolute number density. The *i*-octane profile is plotted relative to its initial concentration. ..28
Figure 17. FR measurements in of DME oxidation at *T* = 650 K, *P* = 13 bar, and τ_{max} = 0.1 s. The measured profiles of OH and H_2O_2 are plotted vs. axial injector position in units of absolute number density. The DME profile is plotted relative to its initial concentration. 29

LIST OF TABLES

Table 1: Baseline fuel oxidation mechanisms, simulation conditions, and the number of clone mechanisms. 11

This page left blank

ACRONYMS AND DEFINITIONS

Abbreviation	Definition
RH	Hydrocarbon
R	Alkyl radical
ROO	Peroxy radical
QOOH	Hydroperoxyalkyl radical
T	Temperature
P	Pressure
IDT	Ignition delay time
LLNL	Lawrence Livermore National Laboratory
NUIG	National University of Ireland, Galway
LPR	Laser photolysis reactor
FR	Flow reactor
CNN	Convolutional neural net
DNN	Dense neural net
CV	Cross-validation
RMS	Root-mean-square
FAGE	Fluorescence Assay by Gas Expansion
HPFR	High-pressure flow reactor
MFC	Mass flow controller
PID	Proportional-integral-derivative (control loop)
SS	Stainless steel
OD	Outer diameter
ID	Inner diameter
LIF	Laser-induced fluorescence
RGA	Residual gas analyzer
Nd:YAG	Neodymium-doped yttrium aluminum garnet
FWHM	Full width at half max
PMT	Photomultiplier tube
DME	Dimethyl ether

1. INTRODUCTION

Autoignition is important in spark and compression ignition engines,[1, 2] and susceptibility to autoignition is a key factor in fuel performance. Given the diversity of emerging fuel candidates, [3] considerable efforts are underway to classify fuels using high-throughput measurements [4-6] or structure-property relationships. [7-9] The purpose of this project is to design a simple, rapid, low-volume laboratory experiment to assess the autoignition propensity of candidate fuels using measurements of chemical intermediates during dilute fuel oxidation reactions.

Autoignition occurs at low temperatures ($T \leq 900$ K) and is sensitive mainly to oxidation reactions, rather than to fuel decomposition. [10, 11] Figure 1 shows schematically the initial steps in autoignition. Hydroxyl radicals, OH, abstract H atoms from the fuel, RH, to form carbon-centered radicals, R, which can undergo a series of oxygen additions, isomerizations and bond scissions to potentially yield more than one OH per each initiating OH (radical chain branching), thereby contributing to even faster fuel consumption. Radical intermediates, including alkylperoxy, ROO, and hydroperoxyalkyl, QOOH, can divert flux from the autoignition cycle to form relatively unreactive HO_2, inhibiting fuel consumption. However, at some conditions the reactions of HO_2 with the fuel can become the dominant route to radical chain propagation.

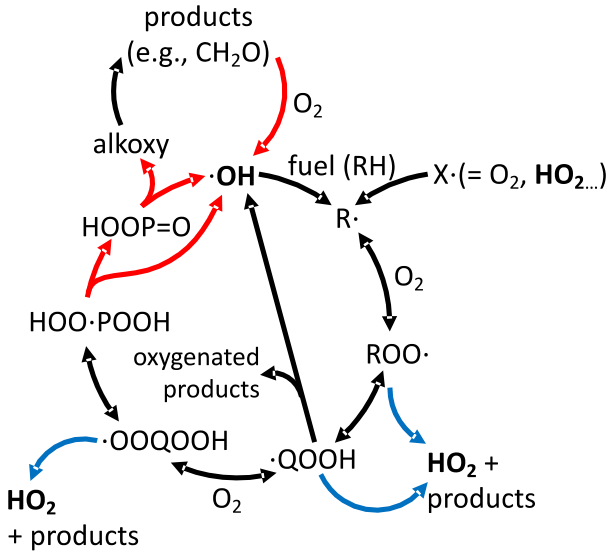

Figure 1: Key elementary reactions in autoignition. Radical chain branching steps are shown as red arrows, chain propagating steps in black, and chain inhibition steps in blue.

Although the rates and product branching of the individual steps shown in Figure 1 depend on the chemical structure of the fuel, OH and HO_2 are always key intermediates, and the propensity of a fuel to form OH versus HO_2 may be a universally good predictor of its overall reactivity. Formaldehyde, CH_2O, is a ubiquitous intermediate in autoignition, and CO_2 is the product of combustion of all hydrocarbon fuels. The present report is divided into two major sections. In section 2 we shows by computational means that measurements of OH, HO_2, CH_2O, or CO_2 from low-T oxidation of very dilute fuel/air mixtures (~1000 times less fuel than in typical engines) can predict reactivity at engine-relevant conditions without detailed knowledge of a complete chemical mechanism. Section 3 describes the design and construction of an experimental apparatus to perform such measurements and the results of preliminary experiments on three

canonical hydrocarbon fuels: *n*-heptane, *i*-octane, and dimethyl ether.

2. PREDICTION OF 1ST-STAGE IGNITION DELAYS BASED ON CHEMICAL KINETICS MODELING

As proof of principle, our goal was to demonstrate that reactivity measurements in a dilute laboratory reactor can be used to predict 1st-stage ignition delay times (IDTs) – common metrics of fuel reactivity at engine conditions. To accomplish this, we used automated chemical modeling and sensitivity analysis to simulate extensive datasets of dilute reactivity measurements and IDTs. We then applied statistical analysis methods to search for a predictive correlation between the simulated measurements and simulated 1st-stage IDTs. This computational approach enabled us to explore different types of hypothetical measurements (e.g. target species, reactor configurations), as described below. Our strategy and results were also published as a peer-reviewed paper in the journal *Combustion and Flame* in 2020.[12]

2.1. Computational strategy

2.1.1. Generation of simulation dataset

We sought to generate a sufficiently diverse simulation dataset of hypothetical fuels to reveal complex trends that are independent of fuel molecular structure. This dataset had to represent a range of fuel structures and functional groups that lead to different reactivities. Unfortunately, there are few literature fuel oxidation mechanisms that are validated at autoignition conditions. Although these mechanisms fall into diverse fuel classes (alkanes, alkenes/aromatics, oxygenates and blends), there are not enough of them to constitute a large dataset on which to base chemical kinetics simulations. To address this challenge, we created synthetic ("clone") mechanisms, based on a subset of "baseline" mechanisms, which we considered to be well validated at $T \leq$ 900 K. These baseline mechanisms, including 18 pure compounds and 5 reference fuel blends, are listed in
Table 1. Whenever possible, we employed widely-used mechanisms from Lawrence Livermore National Laboratory (LLNL) [13] and National University of Ireland Galway (NUIG) [14].

To generate clone mechanisms, we first simulated the proposed dilute oxidation experiments as well as 1st-stage IDTs of each baseline fuel or blend using the CHEMKIN-Pro version 17.2 program package. [15] Next, we identified sensitive reactions and ranked them by their impact on the desired experimental observables. Finally, we systematically perturbed the most sensitive reaction rate coefficients of the baseline mechanisms by factors of two individually or in random pairs. All chemical modeling, sensitivity analysis, and mechanism perturbation was performed via automated workflow that makes use of PyChemkin, [16] a set of scripts that serve as a Python interface to CHEMKIN. The resulting clone mechanisms can be thought of either as entirely new mechanisms that simulate new hypothetical fuels, or simply as perturbations of the original mechanisms within their likely uncertainties. In machine learning analysis, this approach to building large datasets is a form of data augmentation, wherein a small yet reliable dataset is expanded to a larger one by making well-chosen perturbations to the original data. [17] A total of 5296 clone mechanisms was created, from which thousands of unique simulation pairs of dilute reactivity measurements and IDTs could be run. The T and P range of simulations is included in Table 1.

Table 1: Baseline fuel oxidation mechanisms, simulation conditions, and the number of clone mechanisms.

Class	Baseline Fuel	T (K)	P (Bar)	# Clones	Ref.
Alkanes	*n*-Pentane	650 – 700	10	29	[18]
	i-Pentane	650 – 700	10	59	[18]
	neo-Pentane	650 – 700	10	22	[18]
	n-Heptane	650 – 700	13.5 – 40	421	[19, 20]
	i-Octane	700	40	53	[21]
	Cyclohexane	650 – 700	12.5	75	[22]
	Methylcyclohexane (MCH)	650 – 700	15	228	[23]
Alkenes/ Aromatics	1-Butene	700	30	62	[24]
	i-Butene	700	30	43	[25]
	1-Hexene	650 – 700	10	104	[26]
	2-Hexene	650 – 700	10	51	[26]
	Butylbenzene	700	30	51	[27]
Oxygenates	1-Butanol	700	20	12	[28]
	i-Pentanol	650 – 700	20	67	[29]
	Dimethyl Ether (DME)	650 – 700	13 – 40	183	[30]
	Dimethoxy Methane (DMM)	600 – 700	10 – 40	87	[31]
	Tetrahydrofuran (THF)	650 – 700	7	71	[32]
	Methyl Decanoate	650 – 700	12	215	[33]
Blends	PRF	650 – 700	15	778	[26]
	TRF	650 – 700	15	313	
	TPRF	650 – 700	15	1515	
	EPRF	650 – 700	15	448	
	ETPRF	650 – 700	15	409	
Total				5296	

2.1.2. Choosing an experimental platform for dilute oxidation measurements

We first employed our modeling approach to choose the best experimental platform for the proposed dilute reactor. Using CHEMKIN-Pro, [15] we simulated measurements in two common

reactors in chemical kinetics research: a laser photolysis reactor (LPR) and a flow reactor (FR).

In an LPR, [34] a dilute homogeneous gas sample flows through a constant-T and P vessel. Reactions are initiated by laser photolysis of a radical precursor, added in small concentrations to the fuel/air mixture, and the chemical composition is measured as a function of time elapsed after the initiating laser pulse. We modeled the LPR as a constant T and P, homogeneous batch reactor, containing O_2, dilute fuel, and Cl_2 in a balance of N_2. We simulate photolysis of Cl_2 by introducing a known concentration of Cl atoms at time $t = 0$. Cl atoms rapidly abstract H atoms from the fuel and create radicals, which are subsequently oxidized. The simulations output the concentration profiles for all chemical species as a function of post-photolysis time delay. However, we found that unanticipated reactions of Cl with O_2 interfered with fuel oxidation chemistry, which resulted in poor correlations with 1st-stage IDTs, as described in more detail in [12]. Because of this, we consider the LPR to be unsuitable for the proposed measurements of dilute fuel reactivity.

In an FR, a plug of a radially homogeneous gas mixture reacts as it flows in the axial direction for a set residence time, τ, after which the chemical composition is analyzed. [35-42] Different residence times can be obtained either by varying the physical length between the point where reagents are introduced and the probing/sampling position, or by adjusting the total flow velocity through the reactor. We model the FR as a constant T and P, homogeneous plug flow reactor with a maximum residence time, τ_{max}. The modeled gas mixture consists of air (21% O_2 and 79% N_2) and a fixed small amount of fuel (typically $3.2 \cdot 10^{15}$ molecules·cm^{-3}, equal to 0.1 Torr at 300 K). The output of the simulations are the concentrations of each chemical species in the reacting mixture as a function of τ. FR simulations produced good correlations with 1st-stage IDTs, and for the remainder of this project we focused on the FR as the appropriate experimental platform.

2.1.3. Simulations of 1st-stage IDT

We modeled IDTs from simulated air/fuel mixtures (equivalence ratio $\varphi = 1$) in a homogeneous, adiabatic, constant volume batch reactor, which approximates typical conditions in shock tube and rapid compression machine experiments. [43] Such IDTs can also be used to create "maps" of fuel reactivity as a function of T and P, from which the fuel's overall performance can be predicted for different T and P trajectories during an engine cycle. [44, 45] Fuel concentrations in the IDT simulations were ~3 orders of magnitude higher than in the FR/LPR simulations. The energy released by the oxidation reactions of stoichiometric fuel/air mixtures results in ignition, which is manifested as a large increase in the sample temperature and pressure. The output of this simulation is a pressure trace as a function of time, as well as species profiles. We extracted 1st-stage IDT values from the simulation outputs using the first peak in [OH], which is equivalent to using the inflection point in the pressure profiles prior to the main ignition event [11, 46].

2.1.4. Statistical analysis of correlations

To search for a predictive correlation between simulated reactivity measurements and simulated IDTs we explored a progression of increasingly complex methods: linear regression models, principal component analysis, compressed sensing, and neural net fitting. Overall, convolutional neural net (CNN) fitting produced the best results.

CNN's are used to connect a structured input of high dimensionality (e.g. a 2-D image) with an output of lower dimensionality (e.g. a label of what is contained in the image). [47] At each convolution layer, filters containing a small number of fitted weights are applied to localized

regions of the input data and scanned across the input to generate new images/profiles that are called feature maps, which indicate in what regions of the input data certain features appear. The feature maps are then input to the next convolution layer. After the last convolution layer, the final feature maps are combined with scalar values (e.g. *T* and *P* of the simulation) and converted to a single output value using a dense neural net (DNN).

The CNN fitting approach is shown schematically in Figure 2 for an example case, in which simulated OH and HO_2 radical measurement in a flow reactor are used as neural net inputs. The CNN output is a *predicted* 1st-stage IDT value for a given clone fuel. This output is compared to the *explicitly simulated* 1st-stage ignition delays for the same clone fuel. The baseline mechanisms from which we generated clone mechanisms were primarily validated against IDT measurements. Hence, we expect the simulated IDT results for the clone fuels to be realistic representations of the autoignition of hypothetical fuels, in which key reactions are either faster or slower than in the baseline fuels. The CNN parameters were varied to minimize the difference between the predicted and simulated IDT, and the final goodness of fit was evaluated by its root-mean-square cross-validation (CV) error.

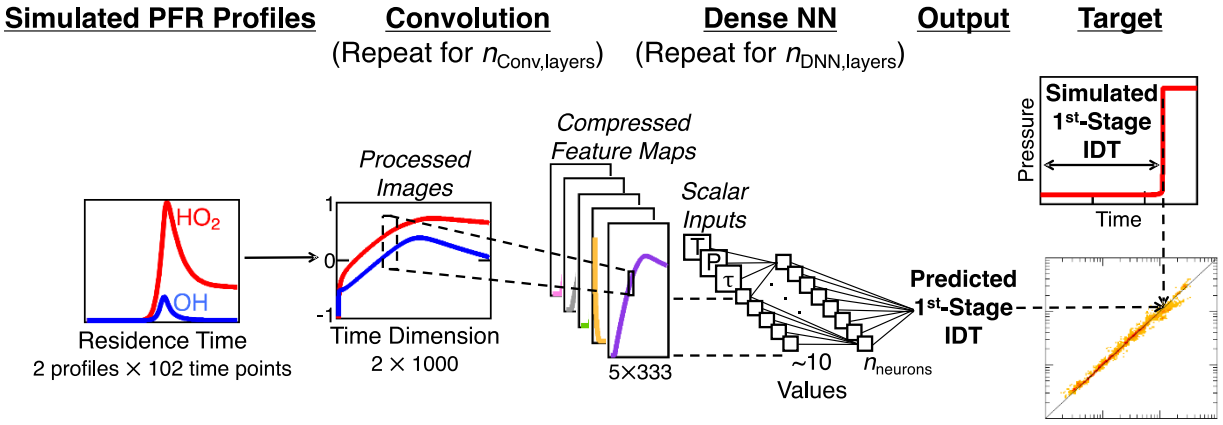

Figure 2: Schematic of CNN architecture used to find correlations between simulated flow reactor profiles and 1st-Stage IDT. The example simulations are for n-heptane at 600 K, 13.5 Bar.

2.2. Results

Typical outputs of our simulations of the FR and IDT measurements are illustrated in Figure 3. The left side presents results for *n*-heptane at P = 13.5 bar and T = 600 K, whereas the right side shows results for *i*-pentanol at 20 bar and 700 K. The top two rows show modeled concentrations of fuel, OH, HO_2, CH_2O, and CO_2 in the FR. The vertical dotted line shows a reactor residence time τ_{SO} at which the fuel begins to spontaneously oxidize, and reaction intermediates begin to appear. The third row plots the rate of production of OH, HO_2, CH_2O, and CO_2 in the FR. The bottom rows depict the fuel concentration and pressure time trace at stoichiometric conditions (φ = 1) in air, from which IDT values are obtained.

2.2.1. Sorted cross-validation error test

Our first approach to neural net fitting involved training and test sets that were randomly chosen from all PFR/IDT simulations. This random CV test produced good agreement of predicted vs.

simulated IDTs. However, we were concerned that random test sets may result in overfitting of the simulations and may appear accurate yet produce no useful correlation.

To guard against overfitting, we employed a 10-fold sorted CV test. Briefly, we ran 13004 unique PFR/IDT simulations and sorted them into 10 equal batches in the order of increasing 1st-stage IDT. We then trained the CNN 10 times (folds). Each fold used one of the batches as test data and the other nine batches as training data. In other words, fold 1 trained the CNN on the least reactive 90% of the simulations (i.e. with largest IDT values) and tested the IDT predictions for the most reactive 10% of the simulations. Fold 2 trained the CNN on the least reactive 80% and most reactive 10% the of the simulations, with the test set falling between 10% and 20% in the order of decreasing reactivity, and so on. This approach evaluates the transferability of the correlation to IDT ranges that were not included in CNN training and is less prone to overfitting.

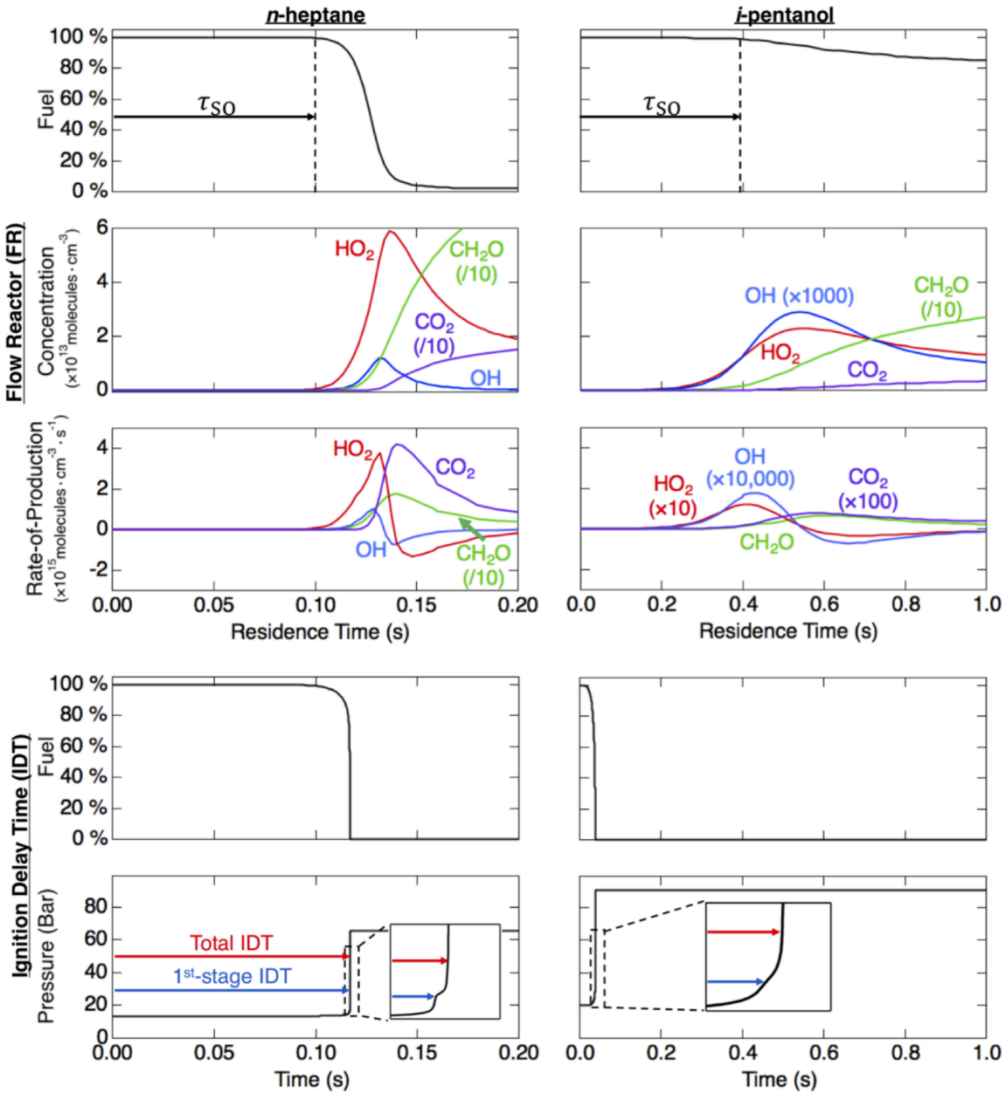

Figure 3. Simulated profiles for oxidation of n-heptane at 600 K and 13.5 bar (left) and i-pentanol at 700 K and 20 bar (right) under flow reactor (top) and ignition delay time (bottom) conditions.

The 10-fold sorted CV test results are shown in Figure 4 as a plot of all predicted vs. explicitly simulated 1st-stage IDTs. The CNN in Figure 4 was trained on OH and HO_2 profiles (CNN's trained on other species profiles are discussed below). The predicted IDTs match the simulated IDTs well, although the agreement varies slightly among the different folds. The overall error distribution is centered on 0% with root-mean-square (RMS) error of only 10.2%, which is comparable to typical reported uncertainties for measured IDTs. [25] Thus, these results suggest that a meaningful correlation exists between the proposed OH/HO_2 measurements in FR and 1st-stage IDT.

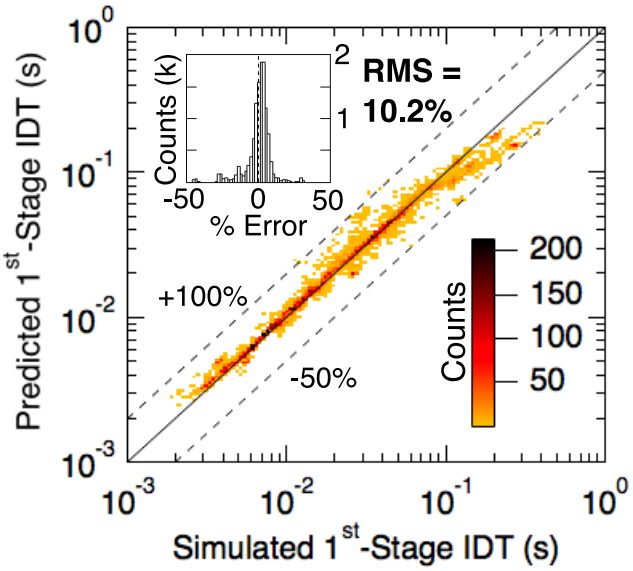

Figure 4: Predicted 1st-stage IDT (from OH/HO_2 FR training data) vs. explicitly simulated 1st-stage IDT. Combined results are shown for the sorted 10-fold CV test, in which the test data consisted of consecutive 10%-wide subsets of all simulations, in order of increasing 1st-stage IDT values (i.e. 0–10%, 10–20%, … 90–100%). Dashed lines represent factor of two errors.

2.2.2. Leave-one-fuel-out test

A key question for our project was whether the correlation, described in Section 2.2.1, is general (i.e. independent of fuel structure). This is difficult to answer because our dataset consists of 23 baseline fuel mechanisms that were each perturbed many times. Therefore, instead of thousands of independent samples, our dataset might instead be 23 distinct clusters of samples, with each cluster subject to its own unique correlation between simulated OH/HO_2 production and IDT. To guard against this possibility, we conducted further tests of CNN fitting, in which all simulations derived from a single baseline mechanism formed a test dataset, with all other simulations used as training data. We repeated these leave-one-fuel-out tests for each baseline mechanism. The summary statistics for each of these tests are shown in Figure 5 for CNN fits using simulated OH and HO_2 profiles (fits to other species are described briefly below). In nearly every case, the leave-one-fuel-out tests predicted 1st-stage IDTs with median errors of a factor of two or less, with THF and 1-butene being the exceptions. Although the agreement is fair overall, it is worse than in the case where all 23 mechanisms are represented in the training and test datasets.

There are two perspectives from which to view these results. On one hand, if we assume that every mechanism faithfully reflects reality, then our correlation may never fully capture some

fuel-dependent details of autoignition. Even so, one can expect to predict 1st-stage IDT within 50% for most fuels, which is sufficient for fuel screening purposes. However, some fuels, like THF and 1-butene, will not be predicted so accurately, and it will be difficult to know *a priori* which fuels exhibit structure-dependent effects. On the other hand, most of our baseline mechanisms are not extensively validated against detailed chemical speciation data and are significantly under-constrained. [48] Because these mechanisms are imperfect, a correlation based on real FR measurements may be better than Figure 5 implies.

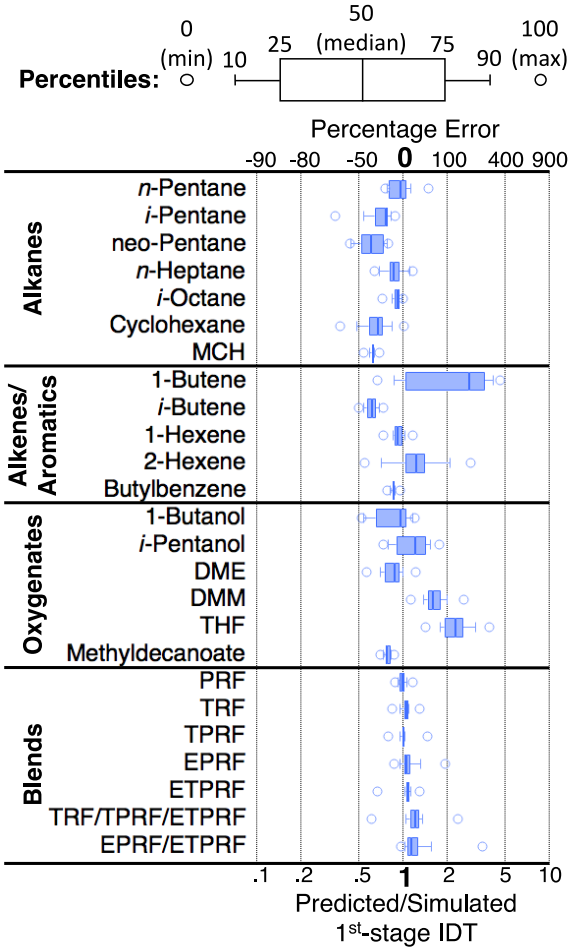

Figure 5: Error distributions of predicted 1st-stage IDTs in the leave-one-fuel-out tests of the FR/IDT simulations. CNN was trained on FR profiles of OH/HO_2.

2.2.3. Choosing an appropriate measurement target

In addition to the OH/HO_2 results discussed above, we optimized CNN fits using simulated CH_2O and CO_2 profiles. Figure 6 plots the sorted CV error of the neural net fits as a function of chemical species being detected. We consider various combinations of species as inputs into the CNN, as well as a case in which no reaction products were detected, but fuel depletion was measured, allowing a determination of τ_{SO}. The CV error ranges from roughly 10 to 14% if the

profiles of any of the simulated species are input to the CNN. If only the fuel depletion is monitored, the CV error is 19.4%.

The clearest conclusion from Figure 6 is that any direct measurement of the overall timescales of spontaneous oxidation (τ_{SO}) of dilute fuel-air mixtures can likely be correlated with autoignition timescales at stoichiometric conditions. If, in addition, residence time profiles of key radical or closed-shell species produced during autoignition are known, the quality of the correlation improves further. Nominally, the best correlation is obtained when OH profiles are the only input (9.7% CV error). Leave-one-fuel-out tests for CH_2O and CO_2 inputs are of similar quality to those for OH and HO_2 inputs in Figure 5. Therefore, all four species are likely useful experimental targets for the prediction of 1st-stage IDT.

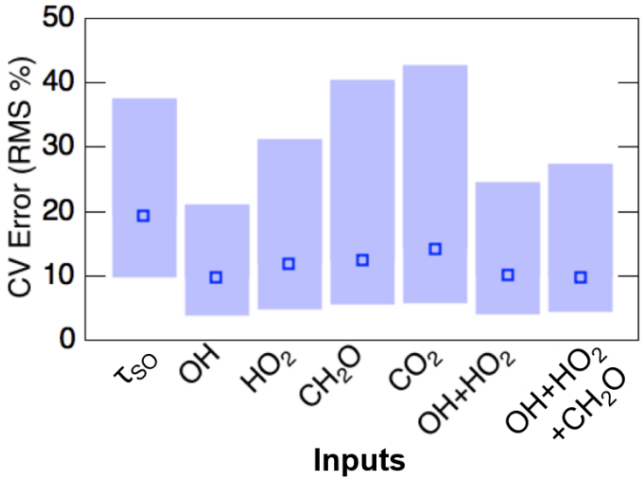

Figure 6: Effect of different inputs to the CNN: markers are 10-fold averaged CV error and the shaded area marks the minimum and maximum test errors of the folds. In the τ_{SO} case the DNN is trained only on T, P and τ_{SO} values, without product profiles input into the CNN.

2.2.4. Optimizing the design of measurements

Finally, we used our modeling approach to estimate how the accuracy of the predicted 1st-stage IDT depends on the design parameters for a hypothetical experiment that measures the concentrations of key combustion intermediates in a flow reactor. Specifically, we considered how the observation time range, fuel dilution, detection sensitivity, and temporal resolution affect the predictive power of the derived correlation. These results are detailed in [12].

Briefly, we found that residence times at least two times larger than τ_{SO} are required. (τ_{SO} is defined as the point at which 1% of the fuel has been consumed, i.e. the start of spontaneous oxidation.) This is an important parameter in designing a flow reactor, because it marks the minimum residence time over which the reacting mixture must maintain well-defined transport properties. Our simulations show that a flow reactor that accommodates residence times of 1 – 2 s should be appropriate for most fuels.

We also found that the perfect FR should operate with ~ 0.1 Torr partial pressure of fuel. Higher fuel concentrations will result in too much heat release, violating the isothermal assumption for the FR. On the other hand, lower fuel concentrations will decrease the predictive quality of the correlation.

The residence time resolution of ~1 ms is optimal. Lower time resolution results in the loss of kinetic information in the detected chemical species profiles and in decreased predictive power of the correlation. Achieving a 1 ms time resolution in a high-pressure FR is an ambitious goal, and our solution to this challenge is discussed in detail in Section 3.1.1.

Lastly, minimum detection sensitivity of ~10^{12} molecules·cm^{-3} or better is required. This targeted detection limit of 10^{12} molecules·cm^{-3} for OH/HO_2 in a high-pressure environment can be achieved for OH using laser-induced fluorescence detection. [49, 50] Additionally, the related technique of fluorescence assay by gas expansion (FAGE) has potential for measurements of OH and HO_2 simultaneously and with similar sensitivity above ambient pressures. [51]

2.3. Summary

Our computational models suggest that a laboratory measurement of OH (and possibly HO_2, CH_2O, or CO_2) concentrations in a dilute flow reactor can be used to predict bulk autoignition properties such as 1st-stage ignition delay times. The following sections describe the design and construction of an experimental apparatus using a high-pressure flow reactor and FAGE detector and initial proof-of-principle attempts at detecting OH and HO_2.

3. CONSTRUCTION OF A HIGH-PRESSURE HPFR/FAGE APPARATUS.

The computations described above identified a promising experimental strategy to measure OH radical concentrations during the oxidation of dilute fuel/air mixtures as a proxy for autoignition propensity of a given fuel or fuel blend. The following section details the construction and commissioning of a laboratory apparatus designed for fuel screening experiments, as shown schematically in Figure 7. The apparatus consists of a heated high-pressure flow reactor (HPFR), operating at engine-relevant conditions, and a Fluorescence Assay by Gas Expansion (FAGE) detector. The FAGE quantifies the concentration of OH and other chemical species as a function of residence time (i.e. reaction time) in the HPFR. Below we report the design, assembly, and calibration of the HPFR/FAGE, along with proof-of-principle experimental measurements of the oxidation of representative hydrocarbon fuels *n*-heptane, *i*-octane, and dimethyl ether.

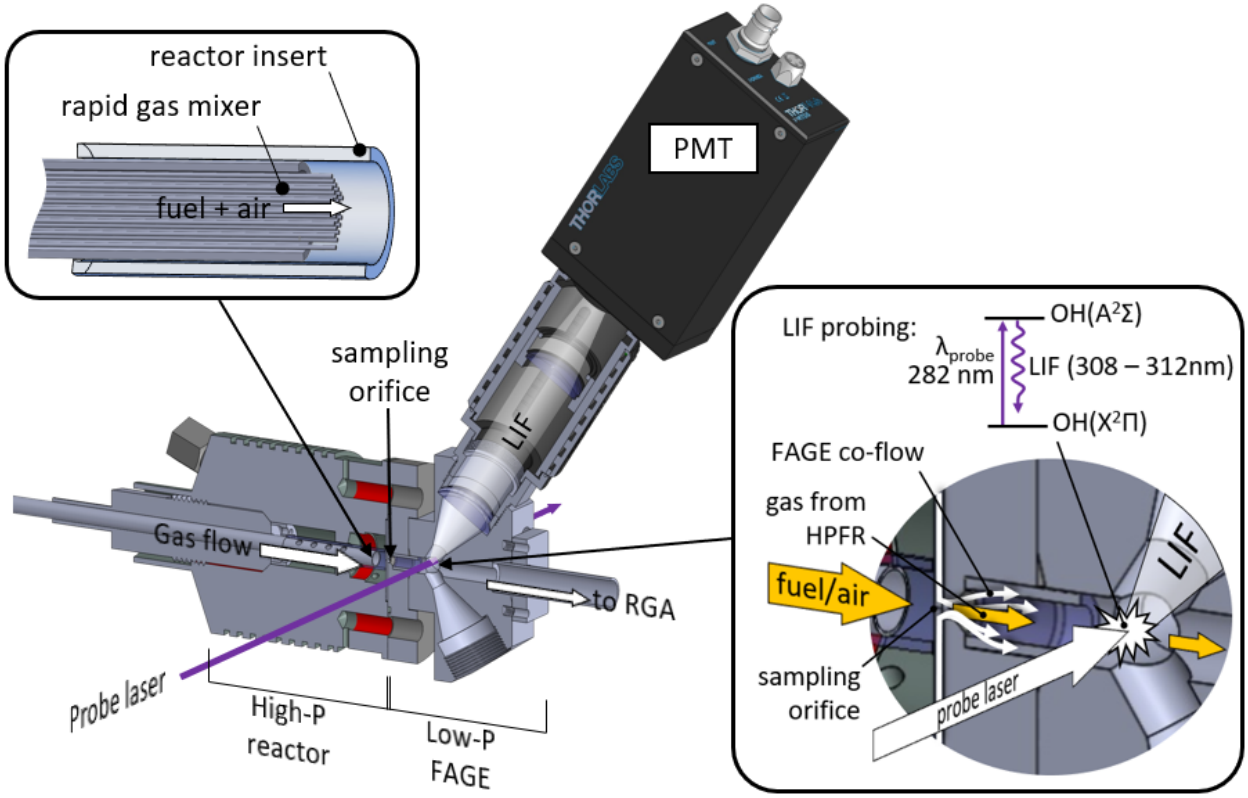

Figure 7. Overview schematic of the HPFR/FAGE apparatus. *Top insert*: cartoon of the rapid fuel mixer in the HPFR. *Right insert*: cartoon of the sampled gas flow and laser-induced fluorescence probing in the FAGE.

3.1. High-Pressure Flow Reactor.

The HPFR is a cylindrical reactor, in which a homogeneous gas mixture is allowed to react for a well-defined time period (τ) at T = 300 – 1000 K and P = 1 – 100 bar. It operates in the laminar flow regime, which we chose because it is easily implemented in chemical kinetics simulation codes. The simple gas transport physics of laminar flows are well understood and enable high-fidelity modeling of the chemistry in the reactor. The HPFR is an Inconel chamber with a 4 cm-long inner bore of 8 mm diameter. The inner bore is lined with an annular insert, ID = 6 mm, OD = 8mm (see inset in Figure 7), that can be made of either Inconel or of Fused Silica, if a more

chemically inert insert is needed. Fuel vapor (diluted in N_2) and air enter the HPFR separately through a custom-built gas mixer, mix together, and flow forward at constant temperature and pressure. The construction of the gas mixer is detailed below. Most of the reacting fuel/air mixture exits the HPFR through six openings, located symmetrically around the circumference of the inner bore at the endwall. A small central portion of the mixture exits the HPFR through an interchangeable laser-drilled orifice in the endwall and enters the FAGE section.

The speed of the fuel/air flows is set by precision mass flow controllers (MFCs, Bronkhorst) to obtain a desired maximum sample residence time in the reactor, τ_{max}. The gas mixer moves axially from fully withdrawn (at the reactor entrance, position x = 38 mm) to fully inserted (at the sampling endwall, x = 0 mm). This translation at constant gas flow speed continuously varies the effective reactor length and hence sample residence time τ: $0 < \tau < \tau_{max}$. A computer-controlled motorized stage moves the mixer without venting the HPFR, which is enabled by a graphite mixer seal with a slip fit. The endwall sampling orifice diameter (typically 0.005 – 0.07 mm) is chosen such that ~10% of the total gas flow is sampled into the FAGE at the desired *T* and *P*.

The HPFR is equipped with three independent resistive heaters: pre-heater located at the gas inlet, main section heater, and front flange heater located at the interface with the FAGE section. Thermocouples sense the gas temperature in three zones: just before the inner bore of the HPFR, at the tip of the gas mixer, and at the exit of the reactor. PID-based current relays control the power output of the heaters to maintain desired temperature throughout the reactor. The main exhaust of the reactor flows to a roots pump, and a PID-controlled throttle valve in the exhaust line maintains desired pressure. Initial fuel concentrations are always small enough that heat released during the complete oxidation process raises the reactor *T* by <5 K.

3.1.1. Construction of the rapid laminar gas mixer

Our chemical kinetics simulations indicate that for the purposes of rapid fuel screening, the HPFR must operate over a wide range or residence times, from 10s of ms to multiple seconds. Achieving the low end of this range of τ is challenging, because it requires reaction initiation times much shorter than τ, i.e. <<10 ms. To address this challenge, we designed a rapid gas mixer, which combines pre-heated fuel and air (unreactive when separate) into a homogeneous reactive sample, while maintaining a laminar flow field. An alternative approach of rapidly heating a pre-mixed fuel/air mixture was found to be not feasible. Fluid dynamics simulations (see below) show that mixing times less than 10 ms are attainable even at high pressures, despite diffusion being slow. To achieve short mixing times, the mixer is made up of many small stainless steel (SS) injector tubes, spaced on a square grid inside a larger SS tube (OD = 6 mm, ID = 5.54 mm). The fuel/N_2 gas flows through the tubes, and the air flows between the tubes. The linear speed of the fuel and air flows are set to be approximately equal. When the two flows combine at the exit of the tubes, complete fuel/air mixing requires diffusion on short length scales of only ~0.1 mm (the ID of the injector tubes), resulting in rapid mixing.

We constructed the gas mixer by spot welding a square SS mesh to the front opening of a 30-cm long SS tube, as shown schematically in Figure 8A. Commercially available hypodermic SS tubes were inserted through the mesh in a checkerboard pattern, protruding by 2 mm out of the mesh. The interstitial space between the needles was filled at the back of the mixer with an epoxy seal. The epoxy plug is sufficiently strong to withstand typical pressure drops across the mixer (< 1 psi), required to flow dilute fuel/N_2 through the hypodermic tubing. The front section

of the mixer resides inside the HPFR and is heated, but the back section is at room temperature, such that the epoxy plug is not damaged by heat. Air enters the mixer through holes, drilled around the circumference of the outer tube. Air diffuses between the hypodermic tubing and flows forward, mixing with the fuel/N_2 at the tip of the mixer. Figure 8B shows the front of the mixer prototype (version 1), made up of 71 hypodermic tubes (ID = 0.15 mm, OD = 0.3 mm), assembled in a 0.36 x 0.36 mm mesh. More recently, we have constructed an improved version 2 of the mixer, in which ~140 hypodermic tubes (ID = 0.11 mm, OD = 0.21 mm) are spaced equally on a 0.28 x 0.28 mm mesh. The more numerous, smaller tubes of the second version provide improved mixing performance.

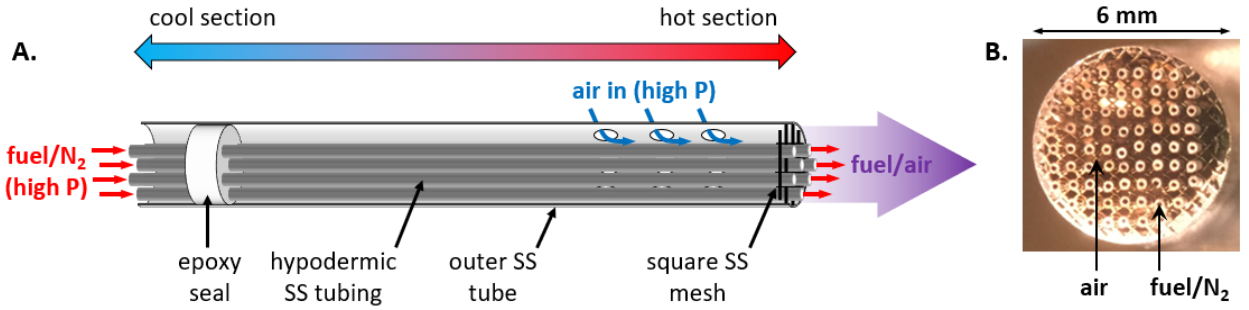

Figure 8. *A*: schematic of the rapid laminar gas mixer. (Dimensions not to scale and only 7 needles are shown for illustration purposes.) *B*: photograph of front of the 1st prototype version of the mixer.

3.1.2. Temperature profile in the HPFR

Our chemical kinetics simulations show that the reactivity of many typical fuels depends strongly on temperature in the autoignition regime, and constant T throughout the reactor is critical to proper modeling of the HPFR results. Figure 9 shows measured centerline temperature profiles in the HPFR for two different maximum residence times and four T setpoints. At each T/τ_{max} combination, we mapped out the temperature profile as a function of axial position at 5 different mixer positions, which correspond to 5 data points in a typical τ scan. To measure these profiles, we inserted an independent thermocouple through a large sampling orifice in the endwall and translated it axially from the mixer (4, 12, 20, 28, and 36 mm) to the endwall (x = 0). These measurements show that the temperature profiles in the HPFR are constant to within ±5 K at slow sample flows (τ_{max} = 1 s) and ±2 K at fast flows (τ_{max} = 0.1 s) and that the profiles do not change appreciably during a τ scan.

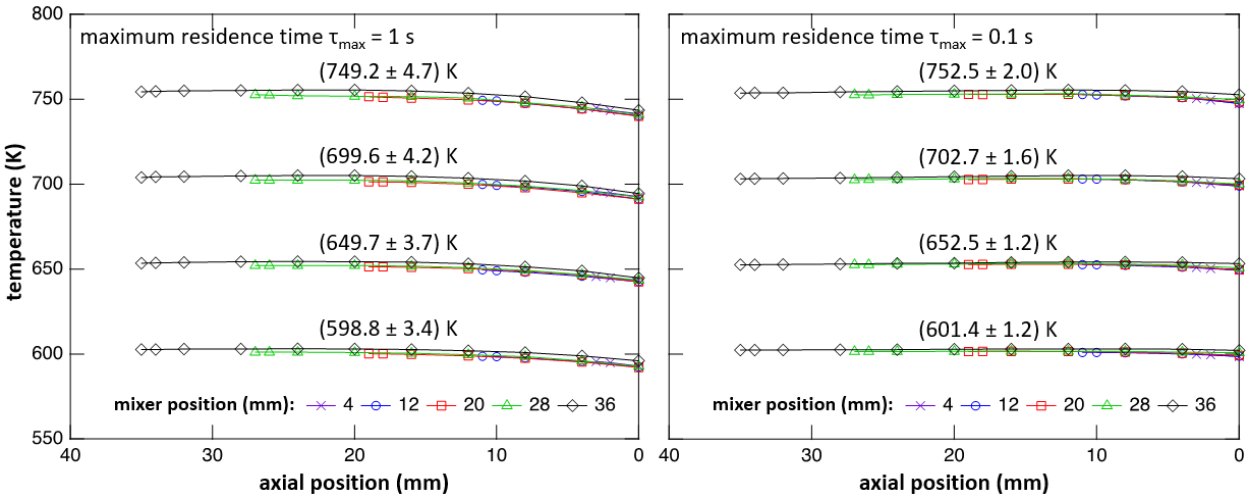

Figure 9. Temperature profiles under typical operating conditions at P = 13 bar in the HPFR with average residence times τ = 1 s (*left*) and 0.1 s (*right*).

3.1.3. Fluid dynamics simulations of the HPFR

We ran 3D simulations of the HPFR in COMSOL [52] to characterize both the expected flow field and the mixing timescale. Figure 10 and Figure 11 show that the simulated flow field strongly resembles a simple "entrance region" model, [53] wherein a flat velocity profile develops into a radially symmetric parabolic profile over a well-known axial distance. Conveniently, the reduced-dimension, 2D entrance region can be modeled in the advanced chemical modeling software CHEMKIN, which enables accurate treatment of both physical transport and complex, detailed chemistry. Figure 10 shows that the 2D CHEMKIN model is a good approximation of the full 3D COMSOL model at two extreme values of τ_{max}. Modeling results shown in section 4 use the 2D CHEMKIN model of the flow field, which is implemented *via* the Cylindrical Shear Flow module with a very thin boundary layer at the reactor entrance.

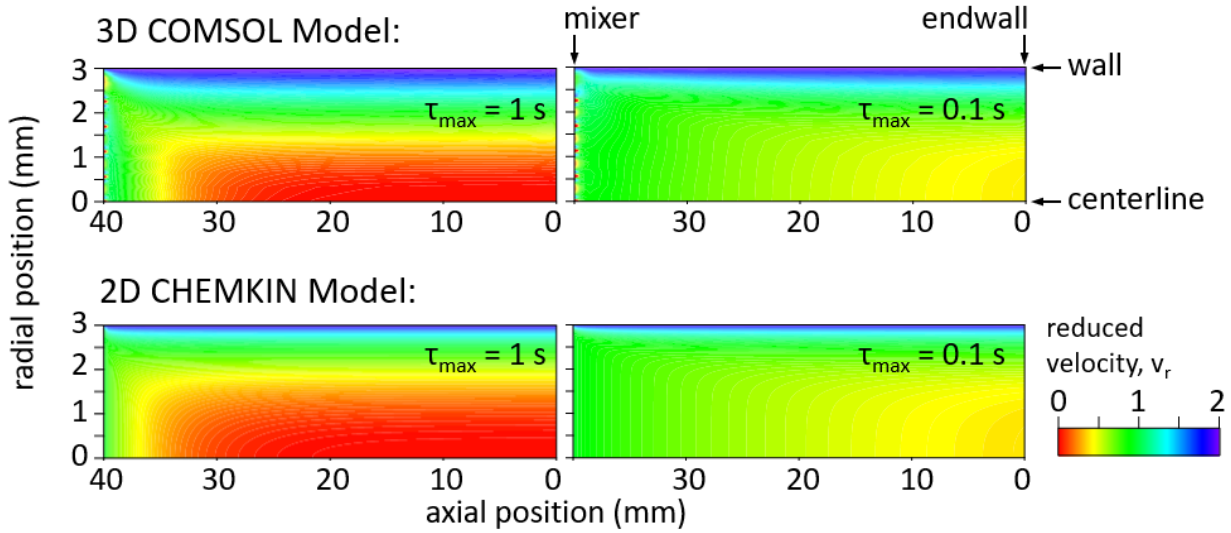

Figure 10. Reduced velocity v_r (defined as the ratio of gas velocity to the average velocity) as a function of the spatial position in the HPFR at P = 13 bar and T = 600 K. The gas flow from the mixer at x = 40 mm to the sampling endwall at x = 0 mm is simulated for τ_{max} = 1 and 0.1 s.

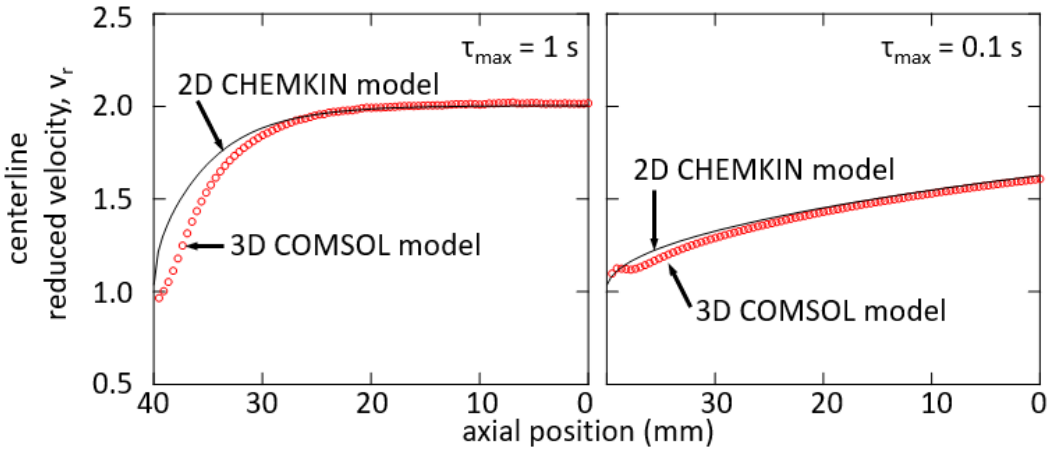

Figure 11. Simulated centerline reduced velocity at P = 13 bar, T = 600 K, τ_{max} = 1 and 0.1 s.

Regarding the mixing timescale, τ_{mlx}, the 3D COMSOL simulations are consistent with back-of-the-envelope estimates for diffusion: at 10 bar and 600 K a typical fuel like n-heptane will be well-mixed in the bulk air flow within ~1 ms. This timescale depends on pressure and temperature through a simple analytical expression: $\tau_{mix} \propto P \cdot T^{-1.75}$. For the low-temperature oxidation chemistry that we hope to observe, a 1 ms mixing time is sufficiently faster than the reaction timescale (10 ms to seconds), such that our subsequent 2D CHEMKIN models assume that the fuel/air streams are well-mixed at the entrance of the HPFR.

3.2. FAGE detector

FAGE instruments are routinely used to detect species, sampled from the atmosphere (i.e. near room temperature, 1 bar pressure) by laser-induced fluorescence (LIF). [51] Our FAGE differs from other existing FAGE setups in two ways: it is 1) capable of analyzing gas, sampled from a heated high-pressure reactor and 2) capable of operating in a time-resolved Photolysis/LIF mode, as detailed below. The purpose of the FAGE here is to measure the concentration of OH and other species of interest in the reacting gas, sampled from the HPFR. The FAGE is a SS chamber (shown schematically in Figure 7) that attaches to the front flange of the HPFR. The sample enters the FAGE through a 1.5 cm-long, 6.2 mm-diameter channel. Four thin channels, machined into the front flange, allow for additional gas (labeled FAGE co-flow in Figure 7) to enter the FAGE and mix with the effluent from HPFR immediately after the sampling orifice. The co-flow inlets are located symmetrically around the sampling orifice, and the amount of co-flow is metered by a dedicated MFC.

The sampled gas traverses the FAGE and exits through a centerline exhaust port. The pressure in the FAGE is controlled by a downstream throttle valve and is typically 5 Torr. We do not actively regulate the temperature in the FAGE. Typically, the front of the FAGE approaches the HPFR temperature and the exhaust section is at room *T*. The FAGE has 4 optical ports: two 4.6 mm-dia. horizontal ports (with Brewster angle windows) orthogonal to the HPFR/FAGE centerline and two 25 mm-dia. off-axis ports directed at 57° up and down in a vertical symmetry plane of the FAGE. The optical ports are used for spectroscopic detection of OH and other

species. In addition, the exhaust port is equipped with a residual gas analyzer (RGA, MKS Instruments), which can be used for the detection of high-concentration species such as the fuel.

3.2.1. FAGE operating modes

There are three operating modes of the FAGE detector:

The ***LIF-only*** mode is used to detect molecules that produce strong fluoresce signals and can be efficiently detected by LIF. In the present report we use this mode to measure steady state OH concentrations in the sampled gas. We have calibrated the OH detection efficiency of our apparatus as described below, enabling absolute OH quantification. A probe laser pulse, directed through the horizontal ports, intersects the sampled gas at 90° and excites the (0,1) band of $A^2\Sigma^+ \leftarrow X^2\Pi$ transition of the OH radical. The probe pulses come from the frequency-doubled output of a Nd:YAG-pumped dye laser at 281.9 nm with duration of 6 ns (FWHM). The LIF signal at 308 – 312 nm from the (1,1) and (0,0) bands of OH is collected through the upper off-axis port using two focusing lenses and a 310-nm bandpass filter with 10-nm bandwidth. The signal is detected with a photomultiplier tube (PMT, Thorlabs), conditioned with a pre-amplifier, and recorded by a 1-GHz digital oscilloscope.

The ***Chemical titration/LIF mode*** detects molecules that do not produce strong LIF signals themselves but can be chemically converted to good LIF targets. A reactant is introduced in the FAGE co-flow and reacts with the effluent from the HPFR after the sampling orifice (without affecting the chemistry in the HPFR). Here, we use this approach to quantify HO_2 radicals by adding NO, diluted in N_2, to the co-flow, as is commonly done by FAGE apparatus. [51] The reaction $HO_2 + NO \rightarrow NO_2 + OH$ titrates HO_2 (which cannot be detected by LIF) to OH, which is then detected by LIF. We have not yet fully calibrated the HO_2 detection efficiency and therefore do not use this mode extensively; however, a demonstration of this capability is included below.

The ***Photolysis/LIF*** mode is used to detect chemical species that do not produce strong LIF signals but can be converted to good LIF targets by laser photolysis. Here we use a "pump" laser pulse with 10 ns duration from an excimer laser to photodissociate H_2O at 193 nm or H_2O_2 at 248 nm (as described in detail in sections 3.2.2 and 3.2.3), both of which produce known yields of OH. A time-delayed, probe laser pulse then detects OH by LIF as described above. The OH concentration is measured as a function of pump-probe delay with ~12-ns resolution.

3.2.2. Calibration of OH detection efficiency.

The $A^2\Sigma^+$ electronic state of OH relaxes primarily by two competing processes: fluorescence and collisional deactivation. Thus, fluorescence yield from excited $OH(A^2\Sigma^+)$ – and hence our detection efficiency – depends on the environment in the FAGE: specifically, on the frequency of collisions and the collision partner. Practically, the best way to calibrate our OH sensitivity is to measure LIF signals from known OH concentrations at the expected FAGE operating conditions. The calibration protocol includes three steps, in which the FAGE operates in the Photolysis/LIF mode.

First, we flow a mixture of H_2O vapor in N_2 (variable partial pressure of H_2O, diluted in total P = 1 bar) through the FAGE chamber. A photolysis laser pulse at 193 nm enters the FAGE through the bottom off-axis port and dissociates H_2O into OH + H. We calculate the absolute concentration of nascent OH immediately after the photolysis pulse using measured photon flux at 193 nm and the known absorption cross section and OH yield of H_2O. [54] A time-delayed

probe laser pulse at 281.9 nm detects the OH concentration by LIF as a function of delay from the photolysis.

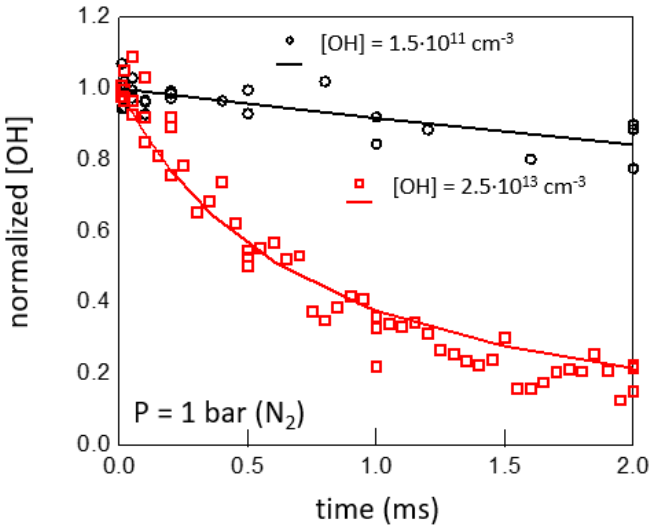

Figure 12. Representative OH time profiles measured using the Photolysis/LIF mode at total P = 1 bar (N_2) in the FAGE. Computed initial OH concentrations are $1.5 \cdot 10^{11}$ and $2.5 \cdot 10^{13}$ cm^{-3}. Solid lines are fits using the chemical model of Zhang et al. [55]

Figure 12 shows two representative OH time profiles in 1 bar of N_2 bath gas, taken with computed initial OH concentrations of $1.5 \cdot 10^{11}$ and $2.5 \cdot 10^{13}$ cm^{-3}. The figure includes fits using the chemical model of Zhang *et al*., [55] shown as solid lines. According to this model, at low [OH] (black symbols) the signal decays mainly due to OH diffusion out of the probe volume; the fitted decay coefficient (which is the only adjustable model parameter) is 78 s^{-1}. At high initial [OH], the signal decays due to diffusion and to radical-radical reactions that consume OH: OH + OH → products and OH + H → products. The model predicts that the observed decay timescale in the high-OH regime is very sensitive to the initial OH concentration, yet no adjustment to the model parameters was needed to reproduce the experimental results. Thus, Figure 12 demonstrates that we can reproducibly create well-known initial populations of OH, which is required for the next step of calibration.

In the second step, we flow a mixture with variable partial pressure of water vapor in 5 Torr total pressure (air) through the FAGE and photolyze this mixture at 193 nm as in step 1. A typical OH time trace at these conditions is shown in Figure 13A as time-integrated PMT signal vs. time after photolysis. At total P = 5 Torr OH diffusion is so rapid that it dominates the observed decays even at high [OH]. Nonetheless, the signal, extrapolated back to $t = 0$ provides the desired calibration of observed PMT signal vs. known initial [OH]. Figure 13B shows the combined result of all calibration measurements at temperatures 300 – 600 K, which enables quantitative determination of absolute concentration of OH in the FAGE.

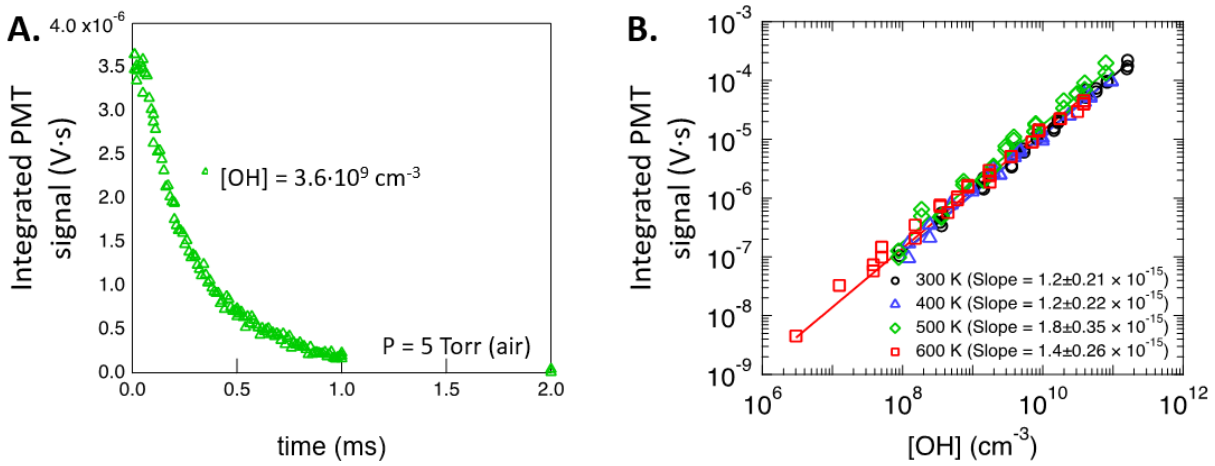

Figure 13. *Panel A*: Typical OH time profile, measured using the Photolysis/LIF mode at total P = 5 Torr (air) in the FAGE. Initial OH concentration is $3.6 \cdot 10^9$ cm^{-3}. *Panel B*: Summary of all OH calibration measurements at *T* = 300 – 600 K.

In the third step, we investigate the transfer efficiency of OH from the HPFR into the FAGE. This is required to account for any possible losses of OH in the sampling process from the HPFR. We replace the gas mixer in the HPFR with an optical window, flow a H_2O/air mixture of known composition through the HPFR, photolyze this mixture directly in the HPFR to produce known [OH], and detect the OH in the FAGE using LIF as before. Figure 14 shows the measured survival probability of OH from the HPFR to the FAGE as a function of the total gas flow rate in the FAGE (sampling + co-flow, at constant P = 5 Torr). At the lowest total flow rate, only ~10% of OH from the HPFR survives into the probe volume of the FAGE. At total flow rate of 600 sccm the residence time in the FAGE is reduced to ~100 μs and co-flow effectively shields the sampled flow from the FAGE walls, resulting in ~100% survival of OH.

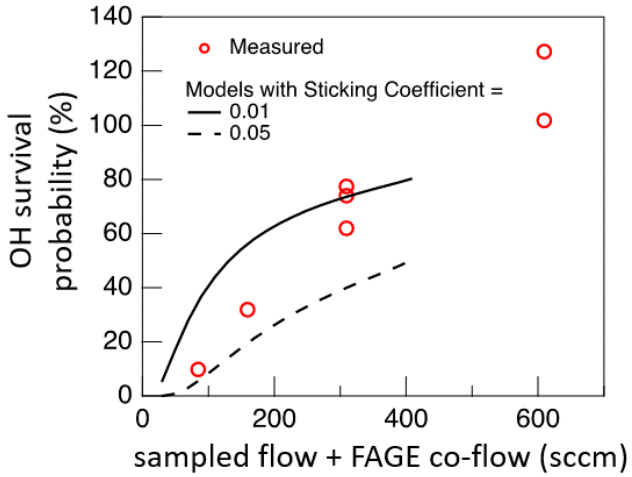

Figure 14. OH survival probability during sampling from HPFR as a function of total gas flow in the FAGE (sampling + co-flow). The survival probability is defined as the percentage of OH radicals, created by laser photolysis in the HPFR, that survive and are detected in the FAGE. Shown for comparison are models of OH transport through the FAGE cell with two values of the sticking coefficient for OH loss on the walls.

The calibration of OH sensitivity is critical to quantitative measurements. The measurements of survival probability of OH in Figure 14 are preliminary and must be repeated. At present, we consider the calibration of total OH sensitivity of the HPFR/FAGE to have uncertainty of a factor of 2. However, with improved measurements we expect this uncertainty to be much smaller.

3.2.3. Subtracting interference in OH measurements at operating conditions

Preliminary experiments in the HPFR revealed OH signals at long residence times (i.e. long after all OH, formed via fuel oxidation, should have decayed). We measured the dependence of these signals on probe laser power to be linear, meaning that these signals were not due to multi-photon OH formation from stable reaction products. Evidently, another process was responsible to conversion of some long-lived reaction products into OH.

Chemical modeling revealed that the only plausible candidate for such process was wall-mediated conversion of H_2O_2 (an abundant, ubiquitous, long-lived, combustion intermediate) into OH. To check for this possibility, we employed the Photolysis/LIF mode, where photolysis laser pulses at 248 nm from an excimer laser were introduced into the bottom off-axis optical port of the FAGE. The absorption cross-section of H_2O_2 at 248 nm is $9 \cdot 10^{-19}$ cm^2, and the OH yield is 2.[56] OH, produced from H_2O_2 photolysis, was quantified by LIF. From this measurement, both the absolute concentration of H_2O_2 and the interfering OH signals due to H_2O_2 were quantified as a function of residence time in the HPFR. The total OH measurements were then corrected for the interfering signals due to H_2O_2.

We note that H_2O_2 is an important combustion intermediate that is challenging to measure experimentally. The capability of our apparatus to quantify H_2O_2 highlights the flexibility of HPFR/FAGE as an experimental platform. Measurements of H_2O_2 will be used in the future as benchmark comparisons with combustion models, on par with OH, HO_2, and other species.

4. FIRST MEASUREMENTS OF REACTIVITY OF REPRESENTATIVE FUELS

For proof-of-principle experimental measurements in HPFR/FAGE, we chose 3 canonical fuels: *n*-heptane, *i*-octane (typical reactive and non-reactive alkanes and primary reference compounds), and dimethyl ether (prototypical oxygenated additive). For each fuel we measured the profiles of 3 species as a function of HPFR residence time: OH *via* LIF-only mode, H_2O_2 *via* Photolysis/LIF mode, and the fuel itself *via* RGA. In the case of *n*-heptane, we also measured HO_2 *via* Chemical titration/LIF mode. All measurements are compared to model predictions using CHEMKIN that rely on the 2D entrance region model for gas transport and two different chemical mechanisms for the detailed chemistry.

4.1. *n*-heptane

As a prototypical reactive reference fuel (Octane Number 0), *n*-heptane is a key benchmark for the HPFR/FAGE. Figure 15 shows measured profiles of *n*-heptane, OH, HO_2, and H_2O_2 using T = 650 K, P = 13 bar, and maximum residence time τ_{max} = 0.2 s, along with model predictions using the Co-Optima [26] and NUIG [20] mechanisms. Qualitatively, all measured species

exhibit the predicted behavior: OH is a short-lived intermediate as manifested by its sharply-peaked profile, HO_2 is a longer-lived intermediate, H_2O_2 is long-lived, and the fuel is rapidly and completely consumed. Furthermore, the injector position (i.e., residence time) at which most of the oxidation occurs is in excellent agreement with the Co-Optima model.

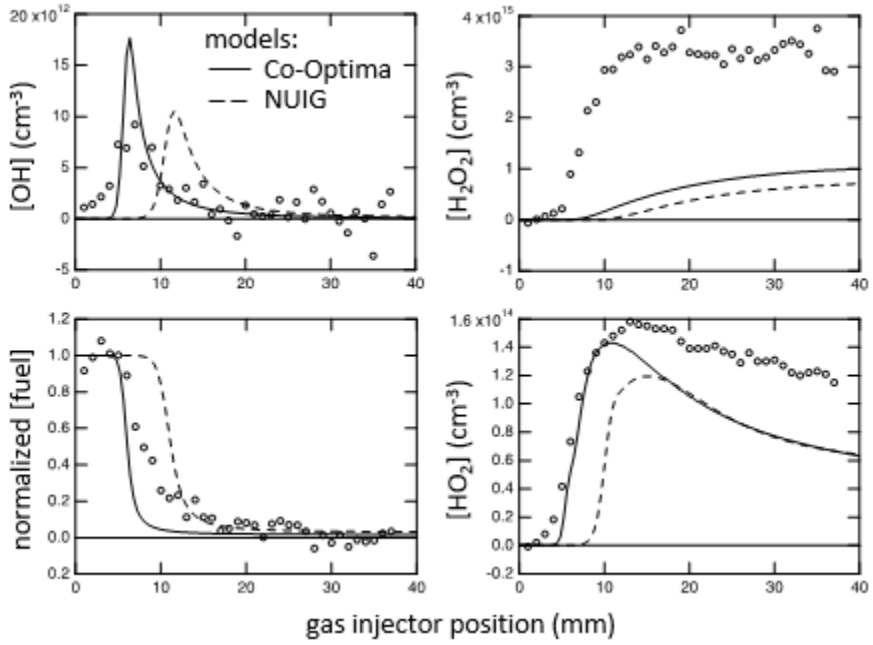

Figure 15. FR measurements in of *n*-heptane oxidation at T = 650 K, P = 13 bar, and τ_{max} = 0.2 s. The measured profiles of OH, HO_2, and H_2O_2 are plotted vs. axial injector position in units of absolute number density. The *n*-heptane profile is plotted relative to its initial concentration.

Quantitatively, the peak OH and HO_2 values agree with the models within the factor of 2 calibration uncertainty. However, HO_2 has additional systematic uncertainty owing to its mode of detection. Although modeling indicates ~50% titration efficiency for HO_2, more experimental characterization is needed and the current agreement with the model may be accidental. H_2O_2 also has additional systematic uncertainty, because we cannot yet fully rule out the possibility of another product being detected *via* photolytic OH production at 248 nm. However, despite expected uncertainties, both models we employed clearly underpredict the observed [H_2O_2], highlighting possible model deficiencies. Overall, the results for *n*-heptane are highly encouraging and demonstrate the capability of the HPFR/FAGE to probe oxidation chemistry in detail on the relevant timescale.

4.2. *i*-octane

Isooctane is the prototypical non-reactive hydrocarbon and a reference fuel with Octane Number of 100. Therefore, it is another important benchmark for the HPFR. Figure 16 compares measurements of *i*-octane, OH, and H_2O_2 at T = 650 K, P = 13 bar, and τ_{max} = 0.5 s with model predictions using Co-Optima and LLNL mechanisms. [21] Most of the comments made on the *n*-heptane data also apply here: the timescale of oxidation agrees with the models as does the peak OH (within the factor of 2 calibration uncertainty), while H_2O_2 is strongly underpredicted by

both models. Unlike *n*-heptane, the fuel is not completely consumed, which is qualitatively predicted by both models and quantitatively matched by the Co-Optima model.

Importantly, the timescale of oxidation for *i*-octane is markedly slower than *n*-heptane (τ_{max} is 0.5 s for *i*-octane vs. 0.2 s for *n*-heptane, thus the observed injector position for peak [OH] corresponds to much longer residence time in *i*-octane experiments). Our results demonstrate that the HPFR/FAGE can clearly resolve the difference between the two fuels and is therefore a powerful potential tool for fuel screening.

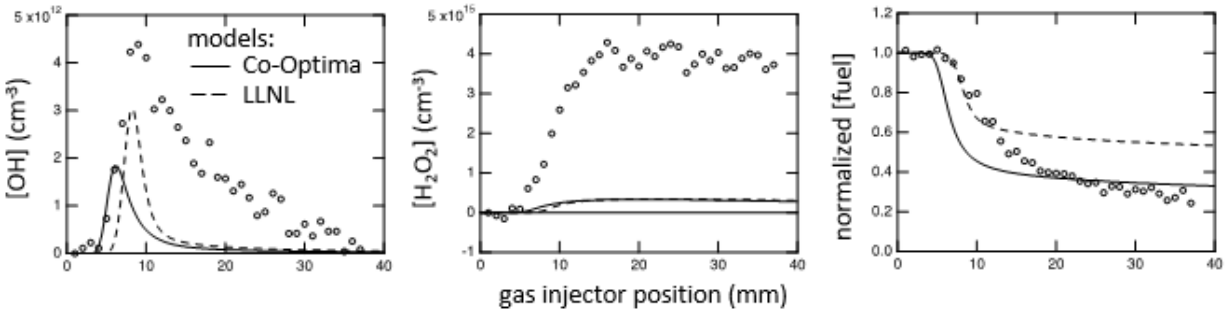

Figure 16. FR measurements in of *i*-octane oxidation at T = 650 K, P = 13 bar, and τ_{max} = 0.5 s. The measured profiles of OH and H_2O_2 are plotted vs. axial injector position in units of absolute number density. The *i*-octane profile is plotted relative to its initial concentration.

4.3. DME

Figure 17 shows the measurements of DME, OH, and H_2O_2 concentrations at T = 650 K, P = 13 bar, and τ_{max} = 0.1 s together with the predictions of the Co-Optima and LLNL [30] models. DME is considered a promising additive or replacement for diesel fuel. It is highly reactive and expected to behave more like *n*-heptane than *i*-octane. Indeed, as shown in Figure 17, a short residence time, τ_{max} = 0.1 s, is needed to resolve the oxidation timescale. Peak OH is underpredicted by more than a factor of 2 by both models. This greater discrepancy, compared with *n*-heptane and *i*-octane, may result from greater uncertainty in the OH calibration: DME experiments were performed at total flow of 150 sccm in the FAGE and thus had to be corrected for the survival probability of OH as shown in Figure 14. (The measurements for *n*-heptane and *i*-octane were performed at ≥ 300 sccm total flow, where the survival probability is nearly 100%.) H_2O_2 is underpredicted by a similar margin as for *n*-heptane and *i*-octane. Finally, the fuel is consumed more gradually than predicted by the model, which could indicate a transport effect at fast flows that is not adequately captured by our 2D physical model. Nonetheless, the measured fraction of leftover fuel (~20%) matches both models well.

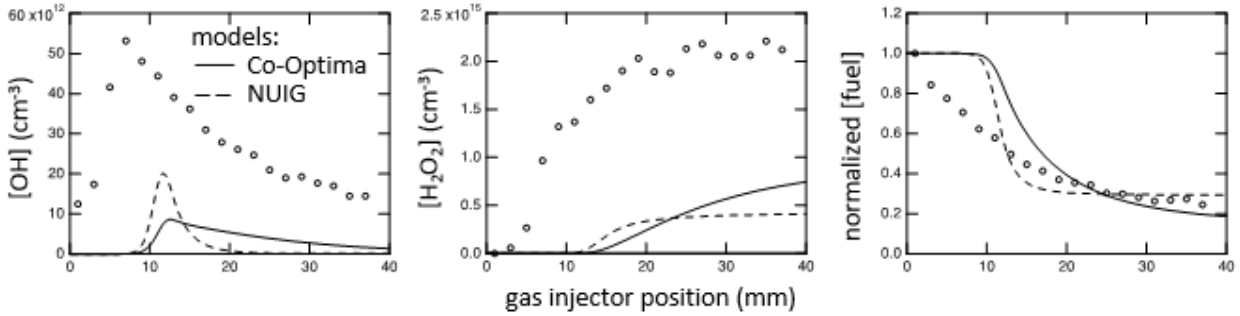

Figure 17. FR measurements in of DME oxidation at T = 650 K, P = 13 bar, and τ_{max} = 0.1 s. The measured profiles of OH and H_2O_2 are plotted vs. axial injector position in units of absolute number density. The DME profile is plotted relative to its initial concentration.

5. CONCLUSION/OUTLOOK

The present report describes the development of an experimental apparatus (HPFR/FAGE), which enables quantitative measurements of important combustion reaction intermediates. These measurements can be compared to model predictions to benchmark theoretical chemical kinetics calculations and advance the frontiers of fundamental chemical science. Importantly, the species that can be measured by the HPFR/FAGE include OH and HO_2, which are notoriously challenging to observe experimentally by conventional techniques, yet which provide potentially the most useful insight into complex reaction networks.

On a more practical level, the HPFR/FAGE experiments can be applied to small amounts of experimental fuel compounds or fuel blends to rapidly assess their autoignition timescale at low-temperature combustion conditions. This report also describes a computational method to correlate these laboratory measurements of autoignition propensity with bulk combustion metrics at engine-relevant conditions. Although such predictive correlations are not yet fully developed, we have created the foundational knowledge base required to bring this computational strategy to fruition. In the future, we hope that the HPFR/FAGE instrument will contribute to both fundamental detailed chemical studies and practical fuel screening efforts.

REFERENCES

[1] Z. Wang, H. Liu, R.D. Reitz, Knocking combustion in spark-ignition engines, Progress in Energy and Combustion Science 61 (2017) 78-112.

[2] J. Dec, Advanced compression-ignition combustion for high efficiency and ultra-low NO_X and soot, in: D. Crolla, D.E. Foster, T. Kobayashi, N. Vaughan (Eds.), Encyclopedia of Automotive Engineering 2014.

[3] P.P. Peralta-Yahya, F. Zhang, S.B. del Cardayre, J.D. Keasling, Microbial engineering for the production of advanced biofuels, Nature 488 (2012) 320.

[4] M. Tao, A. Laich, P. Lynch, P. Zhao, On the Interpretation and Correlation of High-Temperature Ignition Delays in Reactors with Varying Thermodynamic Conditions, International Journal of Chemical Kinetics 50 (2018) 410-424.

[5] N. Naser, S.Y. Yang, G. Kalghatgi, S.H. Chung, Relating the octane numbers of fuels to ignition delay times measured in an ignition quality tester (IQT), Fuel 187 (2017) 117-127.

[6] D.M. Cameron, Autoignition Studies of Gasoline Surrogate Fuels in the Advanced Fuel Ignition Delay Analyzer, Mechanical Engineering, University of Colorado Boulder, 2017.

[7] L.S. Whitmore, R.W. Davis, R.L. McCormick, J.M. Gladden, B.A. Simmons, A. George, C.M. Hudson, BioCompoundML: A General Biofuel Property Screening Tool for Biological Molecules Using Random Forest Classifiers, Energy & Fuels 30 (2016) 8410-8418.

[8] S.R. Daly, K.E. Niemeyer, W.J. Cannella, C.L. Hagen, Predicting fuel research octane number using Fourier-transform infrared absorption spectra of neat hydrocarbons, Fuel 183 (2016) 359-365.

[9] K. Dussan, S.H. Won, A.D. Ure, F.L. Dryer, S. Dooley, Chemical functional group descriptor for ignition propensity of large hydrocarbon liquid fuels, Proceedings of the Combustion Institute 37 (2019) 5083-5093.

[10] J. Zádor, C.A. Taatjes, R.X. Fernandes, Kinetics of elementary reactions in low-temperature autoignition chemistry, Progress in Energy and Combustion Science 37 (2011) 371-421.

[11] S.S. Merchant, C.F. Goldsmith, A.G. Vandeputte, M.P. Burke, S.J. Klippenstein, W.H. Green, Understanding low-temperature first-stage ignition delay: Propane, Combustion and Flame 162 (2015) 3658-3673.

[12] Z.J. Buras, C. Safta, J. Zádor, L. Sheps, Simulated production of OH, HO_2, CH_2O, and CO_2 during dilute fuel oxidation can predict 1st-stage ignition delays, Combustion and Flame, (2020).

[13] LLNL, https://combustion.llnl.gov/mechanisms.

[14] NUIG, http://www.nuigalway.ie/combustionchemistrycentre/mechanismdownloads/.

[15] CHEMKIN-PRO 17.2, Reaction Design, San Diego, 2016.

[16] PyChemkin, https://github.com/GreenGroup/PyChemkin.

[17] D. Ho, E. Liang, I. Stoica, P. Abbeel, X. Chen. Population Based Augmentation: Efficient Learning of Augmentation Policy Schedules. In: Proceedings of the 36th International Conference on Machine Learning; 2019; Long Beach, CA. p.

[18] J. Bugler, B. Marks, O. Mathieu, R. Archuleta, A. Camou, C. Grégoire, K.A. Heufer, E.L. Petersen, H.J. Curran, An ignition delay time and chemical kinetic modeling study of the pentane isomers, Combustion and Flame 163 (2016) 138-156.

[19] M. Mehl, W.J. Pitz, C.K. Westbrook, H.J. Curran, Kinetic modeling of gasoline surrogate components and mixtures under engine conditions, Proceedings of the Combustion Institute 33

(2011) 193-200.
[20] K. Zhang, C. Banyon, J. Bugler, H.J. Curran, A. Rodriguez, O. Herbinet, F. Battin-Leclerc, C. B'Chir, K.A. Heufer, An updated experimental and kinetic modeling study of n-heptane oxidation, Combustion and Flame 172 (2016) 116-135.
[21] H.J. Curran, P. Gaffuri, W.J. Pitz, C.K. Westbrook, A comprehensive modeling study of iso-octane oxidation, Combustion and Flame 129 (2002) 253-280.
[22] E.J. Silke, W.J. Pitz, C.K. Westbrook, M. Ribaucour, Detailed Chemical Kinetic Modeling of Cyclohexane Oxidation†, The Journal of Physical Chemistry A 111 (2007) 3761-3775.
[23] W.J. Pitz, C.V. Naik, T.N. Mhaoldúin, C.K. Westbrook, H.J. Curran, J.P. Orme, J.M. Simmie, Modeling and experimental investigation of methylcyclohexane ignition in a rapid compression machine, Proceedings of the Combustion Institute 31 (2007) 267-275.
[24] Y. Li, C.-W. Zhou, H.J. Curran, An extensive experimental and modeling study of 1-butene oxidation, Combustion and Flame 181 (2017) 198-213.
[25] C.-W. Zhou, Y. Li, E. O'Connor, K.P. Somers, S. Thion, C. Keesee, O. Mathieu, E.L. Petersen, T.A. DeVerter, M.A. Oehlschlaeger, G. Kukkadapu, C.-J. Sung, M. Alrefae, F. Khaled, A. Farooq, P. Dirrenberger, P.-A. Glaude, F. Battin-Leclerc, J. Santner, Y. Ju, T. Held, F.M. Haas, F.L. Dryer, H.J. Curran, A comprehensive experimental and modeling study of isobutene oxidation, Combustion and Flame 167 (2016) 353-379.
[26] M. Mehl, S. Wagnon, K. Tsang, G. Kukkadapu, W.J. Pitz, C.K. Westbrook, Y. Tsang, H.J. Curran, N. Atef, M. Al Rachidi, S.M. Sarathy, A. Ahmed, A comprehensive detailed kinetic mechanism for the simulation of transportation fuels, 10th US National Combustion Metting, College Park, MD, 2017.
[27] H. Nakamura, D. Darcy, M. Mehl, C.J. Tobin, W.K. Metcalfe, W.J. Pitz, C.K. Westbrook, H.J. Curran, An experimental and modeling study of shock tube and rapid compression machine ignition of n-butylbenzene/air mixtures, Combustion and Flame 161 (2014) 49-64.
[28] S.M. Sarathy, S. Vranckx, K. Yasunaga, M. Mehl, P. Oßwald, W.K. Metcalfe, C.K. Westbrook, W.J. Pitz, K. Kohse-Höinghaus, R.X. Fernandes, H.J. Curran, A comprehensive chemical kinetic combustion model for the four butanol isomers, Combustion and Flame 159 (2012) 2028-2055.
[29] S. Mani Sarathy, S. Park, B.W. Weber, W. Wang, P.S. Veloo, A.C. Davis, C. Togbe, C.K. Westbrook, O. Park, G. Dayma, Z. Luo, M.A. Oehlschlaeger, F.N. Egolfopoulos, T. Lu, W.J. Pitz, C.-J. Sung, P. Dagaut, A comprehensive experimental and modeling study of iso-pentanol combustion, Combustion and Flame 160 (2013) 2712-2728.
[30] E.W. Kaiser, T.J. Wallington, M.D. Hurley, J. Platz, H.J. Curran, W.J. Pitz, C.K. Westbrook, Experimental and Modeling Study of Premixed Atmospheric-Pressure Dimethyl Ether−Air Flames, The Journal of Physical Chemistry A 104 (2000) 8194-8206.
[31] S. Jacobs, M. Döntgen, A.B.S. Alquaity, W.A. Kopp, L.C. Kröger, U. Burke, H. Pitsch, K. Leonhard, H.J. Curran, K.A. Heufer, Detailed kinetic modeling of dimethoxymethane. Part II: Experimental and theoretical study of the kinetics and reaction mechanism, Combustion and Flame 205 (2019) 522-533.
[32] Y. Fenard, A. Gil, G. Vanhove, H.-H. Carstensen, K.M. Van Geem, P.R. Westmoreland, O. Herbinet, F. Battin-Leclerc, A model of tetrahydrofuran low-temperature oxidation based on theoretically calculated rate constants, Combustion and Flame 191 (2018) 252-269.
[33] O. Herbinet, W.J. Pitz, C.K. Westbrook, Detailed chemical kinetic mechanism for the

oxidation of biodiesel fuels blend surrogate, Combustion and Flame 157 (2010) 893-908.
[34] M.J. Pilling, S.H. Robertson, P.W. Seakins, Elementary radical reactions and autoignition, Journal of the Chemical Society, Faraday Transactions 91 (1995) 4179-4188.
[35] D.N. Koert, N.P. Cernansky, A flow reactor for the study of homogeneous gas-phase oxidation of hydrocarbons at pressures up to 20 atm (2 MPa), Measurement Science and Technology 3 (1992) 607-613.
[36] Z. Lu, J. Cochet, N. Leplat, Y. Yang, M.J. Brear, A high-pressure plug flow reactor for combustion chemistry investigations, Measurement Science and Technology 28 (2017) 105902.
[37] A. Sudholt, L. Cai, H. Pitsch, Laminar flow reactor experiments for ignition delay time and species measurements at low temperatures: Linear alkanes and dimethyl ether, Combustion and Flame 202 (2019) 347-361.
[38] T.B. Hunter, H. Wang, T.A. Litzinger, M. Frenklach, The oxidation of methane at elevated pressures: Experiments and modeling, Combustion and Flame 97 (1994) 201-224.
[39] C.C. Schmidt, C.T. Bowman, Flow reactor study of the effect of pressure on the thermal de-NOx process, Combustion and Flame 127 (2001) 1958-1970.
[40] S.L. Fischer, F.L. Dryer, H.J. Curran, The reaction kinetics of dimethyl ether. I: High-temperature pyrolysis and oxidation in flow reactors, International Journal of Chemical Kinetics 32 (2000) 713-740.
[41] C.L. Rasmussen, J. Hansen, P. Marshall, P. Glarborg, Experimental measurements and kinetic modeling of CO/H2/O2/NOx conversion at high pressure, International Journal of Chemical Kinetics 40 (2008) 454-480.
[42] F. Herrmann, P. Oßwald, K. Kohse-Höinghaus, Mass spectrometric investigation of the low-temperature dimethyl ether oxidation in an atmospheric pressure laminar flow reactor, Proceedings of the Combustion Institute 34 (2013) 771-778.
[43] P. Dagaut, Experiments for kinetic mechanism assessment, in: T. Faravelli, F. Manenti, E. Ranzi (Eds.), Computer Aided Chemical Engineering, Elsevier 2019, pp. 445-471.
[44] D. Lopez Pintor, J. Dec, G. Gentz, Φ-Sensitivity for LTGC Engines: Understanding the Fundamentals and Tailoring Fuel Blends to Maximize This Property, SAE International, 2019.
[45] M. Tao, P. Zhao, D. DelVescovo, H. Ge, Manifestation of octane rating, fuel sensitivity, and composition effects for gasoline surrogates under advanced compression ignition conditions, Combustion and Flame 192 (2018) 238-249.
[46] G. Mittal, M. Chaos, C.-J. Sung, F.L. Dryer, Dimethyl ether autoignition in a rapid compression machine: Experiments and chemical kinetic modeling, Fuel Processing Technology 89 (2008) 1244-1254.
[47] I. Goodfellow, Y. Bengio, A. Courville, Chapter 9: Convolutional Networks, Deep Learning, MIT Press 2016.
[48] N. Hansen, S.S. Merchant, M.R. Harper, W.H. Green, The predictive capability of an automatically generated combustion chemistry mechanism: Chemical structures of premixed iso-butanol flames, Combustion and Flame 160 (2013) 2343-2351.
[49] D. Stone, M. Blitz, T. Ingham, L. Onel, D.J. Medeiros, P.W. Seakins, An instrument to measure fast gas phase radical kinetics at high temperatures and pressures, Review of Scientific Instruments 87 (2016) 054102.
[50] D.J. Medeiros, M.A. Blitz, L. James, T.H. Speak, P.W. Seakins, Kinetics of the Reaction of OH with Isoprene over a Wide Range of Temperature and Pressure Including Direct Observation of Equilibrium with the OH Adducts, The Journal of Physical Chemistry A 122 (2018) 7239-7255.

[51] L. Onel, A. Brennan, M. Gianella, G. Ronnie, A. Lawry Aguila, G. Hancock, L. Whalley, P.W. Seakins, G.A.D. Ritchie, D.E. Heard, An intercomparison of HO_2 measurements by fluorescence assay by gas expansion and cavity ring-down spectroscopy within HIRAC (Highly Instrumented Reactor for Atmospheric Chemistry), Atmos. Meas. Tech. 10 (2017) 4877-4894.
[52] COMSOL Multiphysics, COMSOL, Inc., Burlington, MA, USA.
[53] R.B. Bird, W.E. Stewart, E.N. Lightfoot, Transport Phenomena, John Wiley & Sons 2005.
[54] W.J. Kessler, K.L. Carleton, W.J. Marinelli, Absorption coefficients for water vapor at 193 nm from 300 to 1073 K, Journal of Quantitative Spectroscopy and Radiative Transfer 50 (1993) 39-46.
[55] X. Zhang, M. Sangwan, C. Yan, P.V. Koshlyakov, E.N. Chesnokov, Y. Bedjanian, L.N. Krasnoperov, Disproportionation Channel of the Self-reaction of Hydroxyl Radical, OH + OH → H_2O + O, Revisited, The Journal of Physical Chemistry A 124 (2020) 3993-4005.
[56] G.L. Vaghjiani, A. Ravishankara, Photodissociation of H_2O_2 and CH_3OOH at 248 nm and 298 k: Quantum yields for OH, $O(^3P)$ and $H(^2S)$, Journal of Physical Chemistry 92 (1990) 996-1003.

DISTRIBUTION

Email—Internal

Name	Org.	Sandia Email Address
Technical Library	01977	sanddocs@sandia.gov

This page left blank

This page left blank

Sandia National Laboratories

Sandia National Laboratories is a multimission laboratory managed and operated by National Technology & Engineering Solutions of Sandia LLC, a wholly owned subsidiary of Honeywell International Inc. for the U.S. Department of Energy's National Nuclear Security Administration under contract DE-NA0003525.